



## Article

# Evaluation of Mechanical Properties and Microstructure of X70 Pipeline Steel with Strain-Based Design

Denghui Liu <sup>1,2,3</sup> , Yifan Dong <sup>1</sup>, Rutao Li <sup>1</sup>, Jinxing Jiang <sup>4</sup>, Xiaoyuan Li <sup>2,\*</sup>, Zhenlong Wang <sup>3,\*</sup>  and Xiurong Zuo <sup>1,\*</sup>

<sup>1</sup> Key Laboratory of Material Physics, Ministry of Education, School of Physics and Microelectronics, Zhengzhou University, Zhengzhou 450001, China

<sup>2</sup> School of Electrical and Information Engineering, Zhengzhou University, Zhengzhou 450001, China

<sup>3</sup> School of Life Sciences, Zhengzhou University, Zhengzhou 450001, China

<sup>4</sup> Nanjing Iron & Steel Co., Ltd., Nanjing 210035, China

\* Correspondence: lixiaoyuan@zzu.edu.cn (X.L.); wzl@zzu.edu.cn (Z.W.); zuoxiurong@zzu.edu.cn (X.Z.)

**Abstract:** The microstructure and mechanical properties of X70 pipeline steel with a ferrite/martensite dual-phase microstructure produced by thermo-mechanical controlled processing were investigated by tensile tests, Charpy V-notched (CVN) impact tests, drop-weight tear tests, guided-bend tests, scanning electron microscopy and transmission electron microscopy combined with thermodynamic simulation analysis. All the mechanical properties met the strength, ductility, toughness and deformability properties requirements of X70 grade pipeline steel with strain-based design. The shear fracture area and absorbed energy of CVN at  $-10\text{ }^{\circ}\text{C}$  were  $>97\%$  and  $>205\text{ J}$  in base metal (BM), weld metal (WM) and heat affected zone (HAZ) with low transition temperature, indicating adequate resistance to propagating fracture. The microstructure of WM was mainly intragranular acicular ferrite that can guarantee high strength, toughness and over matching requirements of the welded joint. Because of being exposed to successive heat inputs, the ferrite plus martensite/bainite microstructure of BM was heated between  $A_{c1}$  and  $T_s$  forming the HAZ. However, a high CVN impact toughness of  $345\text{ J}$  at  $-10\text{ }^{\circ}\text{C}$  in HAZ was obtained, which indicated that the excellent mechanical properties of BM would not be seriously deteriorated during the welding thermal cycles with the reasonable addition of Ti and Nb.

**Keywords:** X70 pipeline steel; welded joint; dual-phase microstructure; mechanical properties; Ti; Nb



**Citation:** Liu, D.; Dong, Y.; Li, R.; Jiang, J.; Li, X.; Wang, Z.; Zuo, X.

Evaluation of Mechanical Properties and Microstructure of X70 Pipeline Steel with Strain-Based Design.

*Metals* **2022**, *12*, 1616. <https://doi.org/10.3390/met12101616>

Academic Editor: Ricardo Branco

Received: 29 August 2022

Accepted: 23 September 2022

Published: 27 September 2022

**Publisher's Note:** MDPI stays neutral with regard to jurisdictional claims in published maps and institutional affiliations.



**Copyright:** © 2022 by the authors. Licensee MDPI, Basel, Switzerland. This article is an open access article distributed under the terms and conditions of the Creative Commons Attribution (CC BY) license (<https://creativecommons.org/licenses/by/4.0/>).

## 1. Introduction

In recent years, to meet the varieties of severe environments such as earthquake, landslide, debris flow, etc., pipeline steels are critically required to have not only high strength and toughness but also excellent deformability. By applying ferrite-martensite/bainite microstructural control, high-deformability pipeline steels with strain-based design have been developed [1–3]. The pipeline steels with strain-based design are usually produced by either thermo-mechanical controlled processing (TMCP) [4] or intercritical annealing [5], through which dual-phase microstructure of ferrite-martensite/bainite can be obtained.

Process parameters on microstructure and mechanical properties of pipeline steel with strain-based design were studied in some researches. TMCP is the preferred route because it enables good combination of strength, toughness and deformability to be obtained and, at the same time, keeps the processing cost low. However, ferrite in dual-phase microstructure can be obtained through different TMCP process, which was dynamically transformed from austenite at temperatures above the  $A_{e3}$  transformation temperature [6] or isothermally transformed below  $A_{e3}$ , which the amount of ferrite of the latter can be controlled easily [7,8]. In our previous studies [3,9,10], it is found that intercritical heat treatment followed by rapid water cooling can also achieve dual-phase microstructure with a good combination of deformability, strength and toughness, especially for welded joints.

However, due to high cost, it is necessary to investigate the X70 steel with strain-based design produced by TMCP.

Welding thermal cycles during pipe forming process may change the microstructure and mechanical properties of base metal (BM) forming the heat affected zone (HAZ), which generally degrades the properties and results in the decline of excellent properties of BM [11–13]. The coarse grain HAZ (CGHAZ) adjacent to the weld metal (WM) with large prior-austenite grain boundaries (PAGBs) and coarse martensite-austenite (MA) constituents always have the lowest fracture toughness [12]. However, microalloying element precipitates containing Ti and Nb can prevent the grain growth in CGHAZ in welding thermal cycle [14,15]. Although several studies have been conducted on the properties of the welded joint of pipeline steel, further detailed research on the welded joint of X70 steel with strain-based design is needed to guarantee the rigorous properties requirements after welding.

In this paper, the microstructure and mechanical properties of X70 pipeline steel with a ferrite–martensite/bainite dual-phase microstructure produced by TMCP were investigated. In addition, the microstructural and mechanical properties of the welded joint were also systematically examined by tensile tests, Charpy V-notched (CVN) impact tests, drop-weight tear tests (DWTT), guided-bend tests, scanning electron microscopy, transmission electron microscopy and thermodynamic simulation analysis to further improve the material properties.

## 2. Materials and Methods

One Grade X70 pipeline steel with a diameter of 1016 mm and thickness of 21.0 mm was investigated in this work. Direct reading spectrometer ARL 4460 was used to measure the main chemical composition of the pipe, and the analysis precision can meet the requirement of GB/T 4336–2016. Chemical composition is listed in Table 1. The pipes were formed through a JCOE process. The JCOE process included the crimping of the plate edges, followed by successive forming into a J-shape, C phase and O phase. Both ends of the plate are welded by submerged arc welding with first on the inside and then on the outside. Finally, the plates underwent mechanical expanding [16–18].

**Table 1.** Chemical composition of studied steel (mass%).

Position	C	Mn	Si	Ni	Mo	Nb	Ti	P	S	N	Fe
BM	0.050	1.54	0.20	0.19	0.17	0.059	0.014	0.0198	0.0010	0.0031	Bal.
WM	0.056	1.59	0.33	0.15	0.23	0.028	0.026	0.0170	0.0026	-	Bal.

This pipe was formed using plate that was produced through TMCP with accelerated cooling and had ferrite plus martensite/bainite microstructure. The rolling process took place as follows. The slabs of 260 mm were reheated at 1180 °C in a heating furnace before rolling, in order to obtain sufficient dissolution of carbonitride particles and achieving excellent high temperature thermoplasticity [14]. The rough rolling temperature is about 1110 °C above the recrystallization stopping temperature ( $T_{nr}$ ), and the finishing temperature is about 780 °C below  $T_{nr}$ , and then isothermal holding in the two-phase region of  $A_{r3}$ – $A_{r1}$ , followed by accelerated cooling of 20 °C/S to a temperature of 300 °C. The  $T_{nr}$  was predicted by employing the following empirical Equation (1) [7], which is 1090 °C. The  $A_{r3}$  and  $A_{r1}$  transformation temperature was determined using JMatPro software (Public Release Version 7.0.0, Sente Software Ltd., Guildford, UK), which is 835 °C and 615 °C, respectively.

$$T_{nr} = 887 + 464C + (6645Nb - 664\sqrt{Nb}) + (732V - 230\sqrt{V}) + 890Ti + 363Al - 357Si \quad (1)$$

Tensile tests were conducted at room temperature in both longitudinal and transverse directions according to ASTM A370 (The international standard, American Petroleum Institute), with full-thickness specimens of 38.1 mm in gage wideness and 50 mm in gauge

length on a universal tensile testing machine (CMT5105; SANS, Shenzhen, China). Charpy V-notched (CVN; Wanchen Testing Machine Co., Ltd., Tsingtao, China) impact tests of the BM, weld metal (WM) and HAZ were performed according to ASTM A370 over a range of temperatures from  $-60\text{ }^{\circ}\text{C}$  to  $20\text{ }^{\circ}\text{C}$  to obtain transition curves, with specimens of  $10\text{ mm} \times 10\text{ mm} \times 55\text{ mm}$  size. The orientation was transversal with the notch in weld centerline for WM specimen, with the notch in HAZ for HAZ specimen. Guided-bend tests were carried out in the transversal direction in accordance with ASTM A370. Bending angle is  $180^{\circ}$ . Drop-weight tear tests (DWTT; JL-100000; Shengwei, Shandong, China) were carried out over a range of temperatures from  $-60\text{ }^{\circ}\text{C}$  to  $20\text{ }^{\circ}\text{C}$  in the transversal direction. DWTT specimens have a size of  $300\text{ mm} \times 75\text{ mm} \times \text{thickness}$  in accordance with API RP 5L3 (The international standard, American Petroleum Institute). For each type of test, three test pieces were prepared and tested. Orientations and locations of tensile, impact, and DWTT specimens were shown in Figure 1. According to API Spec 5L, the welded joint was taken from one end of the pipe and subjected to a hardness test in cross section at a load of 10 kgf for 15 s using digital hardness tester (HVS-50 Vickers; Vickers, Shanghai, China). Moreover, hardness test locations for welded pipe included weld centerline, HAZ, and BM, down a straight line with 1.5 mm below the outside surface, as shown in Figure 2.

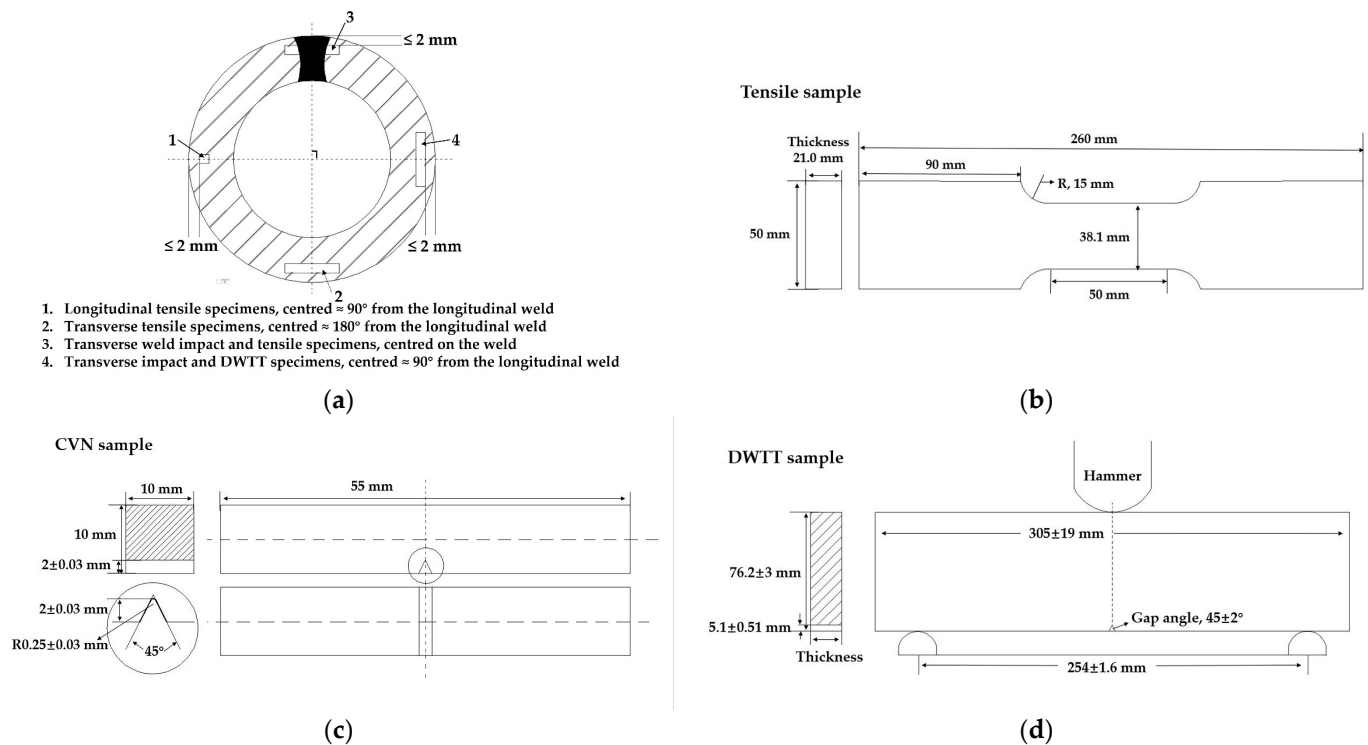


**Figure 1.** Schematic diagram of specimen positions (a) for performance tests and the engineering drawings of tensile (b), impact tests (c) and DWTT (d).

The investigated specimens were ground, mechanically polished and etched in a 4% nital, and then analyzed using scanning electron microscope (SEM; JEOL 6700F, Utah, UT, USA). The more detailed metallographic examination of the pipe was carried out using transmission electron microscopy (TEM; JEM-2100; JEM, JEOL, Tokyo, Japan). For TEM observation, the thin foils were electropolished by a twinjet electro-polisher in a solution of 10% perchloric acid and 90% acetic acid.

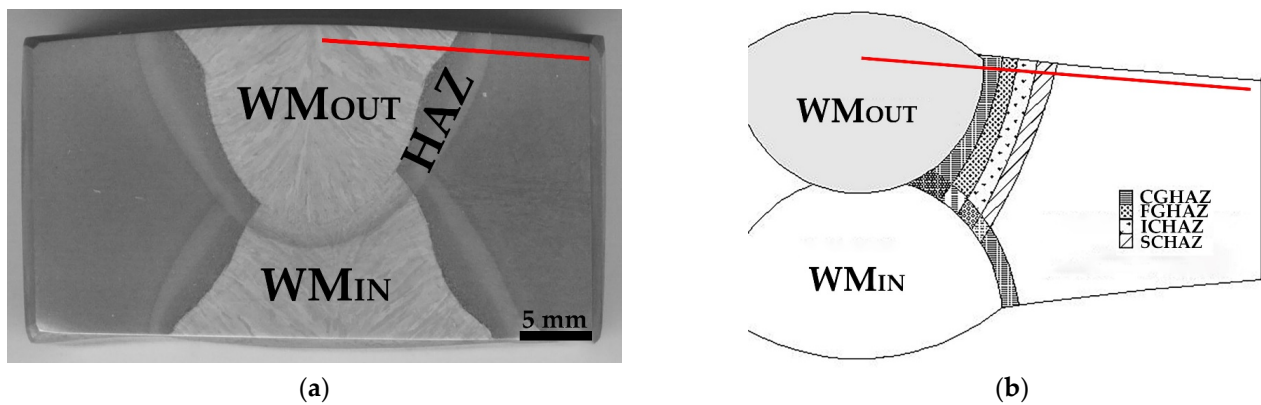


**Figure 2.** Macro morphology (a) and schematic diagram (b) of the welded joint and location marked by red line of hardness tests. The abbreviations in the figure are explained as follows: the heat-affected zone (HAZ), the outside welding (WM<sub>OUT</sub>), the inside welding (WM<sub>IN</sub>), the coarse grain heat-affected zone (CGHAZ), the fine grain HAZ (FGHAZ), the intercritical HAZ (ICHAZ) and the subcritical HAZ (SCHAZ).

### 3. Results

#### 3.1. Mechanical Properties

Figure 3a shows the stress-strain curve of the BM. Tensile properties of the pipe are shown in Table 2. According to the specification of API 5L [19], all the specimens tested in present work met the strength and ductility properties requirements of X70 grade pipeline. As can be seen from Figure 3a and Table 2, BM with a dual-phase microstructure exhibited continuous yielding behavior with an average longitudinal yield strength of 486 MPa, average tensile strength of 642 MPa, average yield ratio of 0.76 and average uniform elongation of 9.4%, indicating high strength and deformability. The yield strength in the transverse direction was higher than that in the longitudinal direction, resulting in the increasing of yield ratio from 0.76 in the longitudinal direction to 0.82 in the transverse direction.

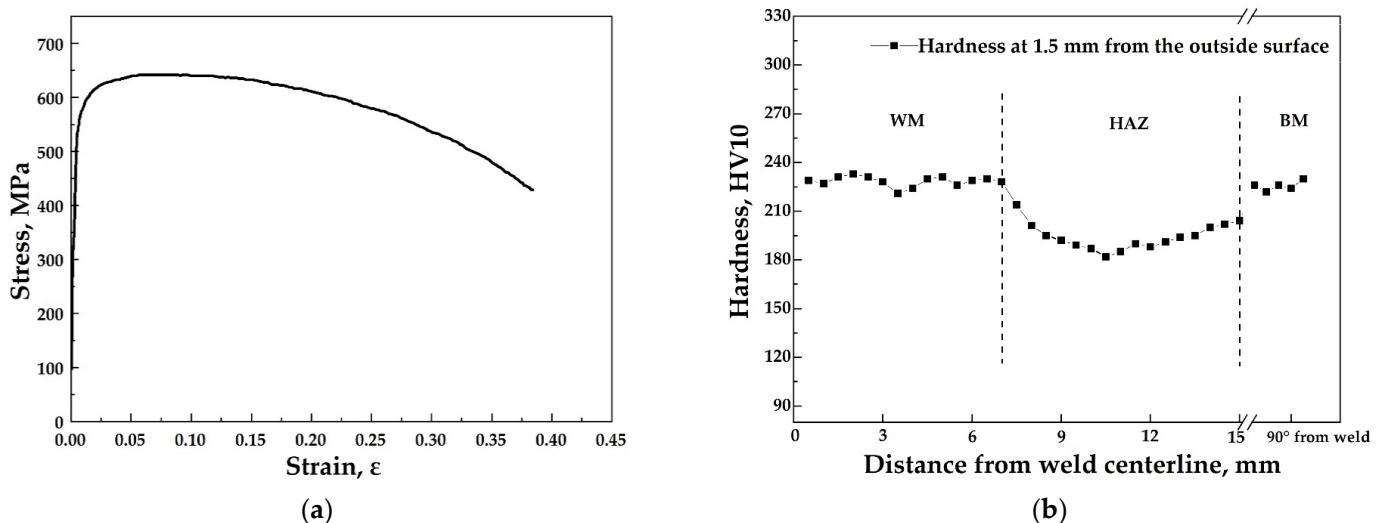


**Figure 3.** Stress–strain curve (a) of the BM, and variation of hardness (b) from weld centerline to BM.

According to the requirements of specification, WM transverse tensile strength higher than 570 MPa and over matching the BM transverse tensile strength are required, and the position of specimen fracture should be in the BM. As shown in Table 2, WM transverse tensile strength was 645 MPa, higher than 630 MPa of BM, meeting the over matching requirement, and the specimens for WM tensile test fractured in the BM, indicating that

strength over matching of the welded joint was obtained. The results of guided-bend tests showed that no cracks occurred in welded joint, showing a good deformation capacity of the welded joint.

**Table 2.** Tensile properties of the pipe.

Specimen	Parameter	Single Value			Average Values	Standard Deviation	Requirements of API Specification
		1	2	3			
BM (L)	Yield strength (MPa)	488	485	485	486	1.4	450–550
	Tensile strength (MPa)	640	640	645	642	2.4	570–715
	Yield ratio	0.76	0.76	0.75	0.76	0.005	<0.85
	Elongation (%)	45	45	44	45	0.5	
	Uniform elongation (%)	9.3	9.4	9.4	9.4	0.047	
BM (T)	Yield strength (MPa)	530	515	500	515	12.2	485–635
	Tensile strength (MPa)	630	630	630	630	0.0	570–760
	Yield ratio	0.84	0.82	0.79	0.82	0.021	
	Elongation (%)	44	46	43	44	1.2	
WM (T)	Tensile strength (MPa)	645	645	645	645	0.0	>570
	Position of fracture	fractured in the BM			Yes	-	

Note: L is the longitudinal; T is the transverse.

Figure 3b shows the variation of hardness from weld centerline to HAZ. As shown in Figure 3b, HV10 hardness in WM was higher than that in HAZ, and decreased rapidly in the CGHAZ, FGHAZ, and ICHAZ, because of microstructural change. In SCHAZ, hardness increased gradually in the direction far from WM.

CVN impact tests of the BM, WM and HAZ were conducted, and the results are showed in Table 3. The results given in Table 3 showed that the CVN absorbed energy and shear fracture area (SA, three specimens for each test) were found to be different for the BM, WM and HAZ. The SA of CVN at  $-10\text{ }^{\circ}\text{C}$  was >97% in the BM, WM, and HAZ. The CVN absorbed energy was >285 J in BM, >315 J in HAZ and >205 J in WM. According to the requirements of specification, the minimum average (of a set of three test pieces) absorbed energy for each pipe weld and HAZ test is 80 J. Meanwhile, individual test values for any test piece shall be  $\geq 75\%$  of the required minimum average (of a set of three test pieces) absorbed energy values, namely 60 J. The WM had the lowest impact energy and SA among the BM, WM, and HAZ, but was still much higher than API X70 requirements, providing sufficient fracture-initiation resistance and sufficient ductile fracture.

**Table 3.** CVN impact properties of the pipe.

Specimen	CVN Absorbed Energy ( $-10\text{ }^{\circ}\text{C}$ ) (J)					Shear Fracture Area ( $-10\text{ }^{\circ}\text{C}$ ) (%)			
	1	2	3	Average Values	Standard Deviation	1	2	3	Average Values
BM	320	285	320	308/286 *	20.2/52.1 *	100	100	100	100
HAZ	315	405	315	345/239 *	52.0/36.7 *	100	100	100	100
WM	240	210	205	218/206 *	18.9/11.1 *	100	97	98	98

Note: \* shows data from the literature [3].

The average CVN absorbed energy of BM, HAZ and WM of the investigated steel produced by TMCP is 22 J, 106 J, and 12 J higher than those produced by intercritical annealing in reference [3]. DWTT SA of BM is also higher in the former than that in the latter. It may be concluded that the cryogenic toughness of the welded joint studied in the experimental steel are significantly better than those produced by intercritical annealing in reference [3].

Figure 4 shows the series CVN and DWTT curves of BM, WM, and HAZ. The fracture-appearance transition temperature of 50% SA by CVN (FATT50CVN) of all specimens was

lower than  $-60\text{ }^{\circ}\text{C}$ . WM already entered the transition range at  $-40\text{ }^{\circ}\text{C}$ , whereas BM and HAZ still stayed on the upper shelf from  $20\text{ }^{\circ}\text{C}$  down to  $-60\text{ }^{\circ}\text{C}$ . The scatter of the data was small in BM and WM, while large for HAZ. The large scatter of the data for the HAZ was due to microstructural heterogeneity. The fracture-appearance transition temperature of 85% SA by DWTT (FATT85DWTT) of BM was  $-38\text{ }^{\circ}\text{C}$ , and DWTT SA was 100% at the test temperature higher than  $-20\text{ }^{\circ}\text{C}$  (Figure 4c). As can be seen from above results, the investigated pipe had adequate resistance to fracture with low transition temperature. Adequate CVN toughness and adequate DWTT SA ensured the avoidance of brittle fracture propagation and the control of ductile fracture propagation.

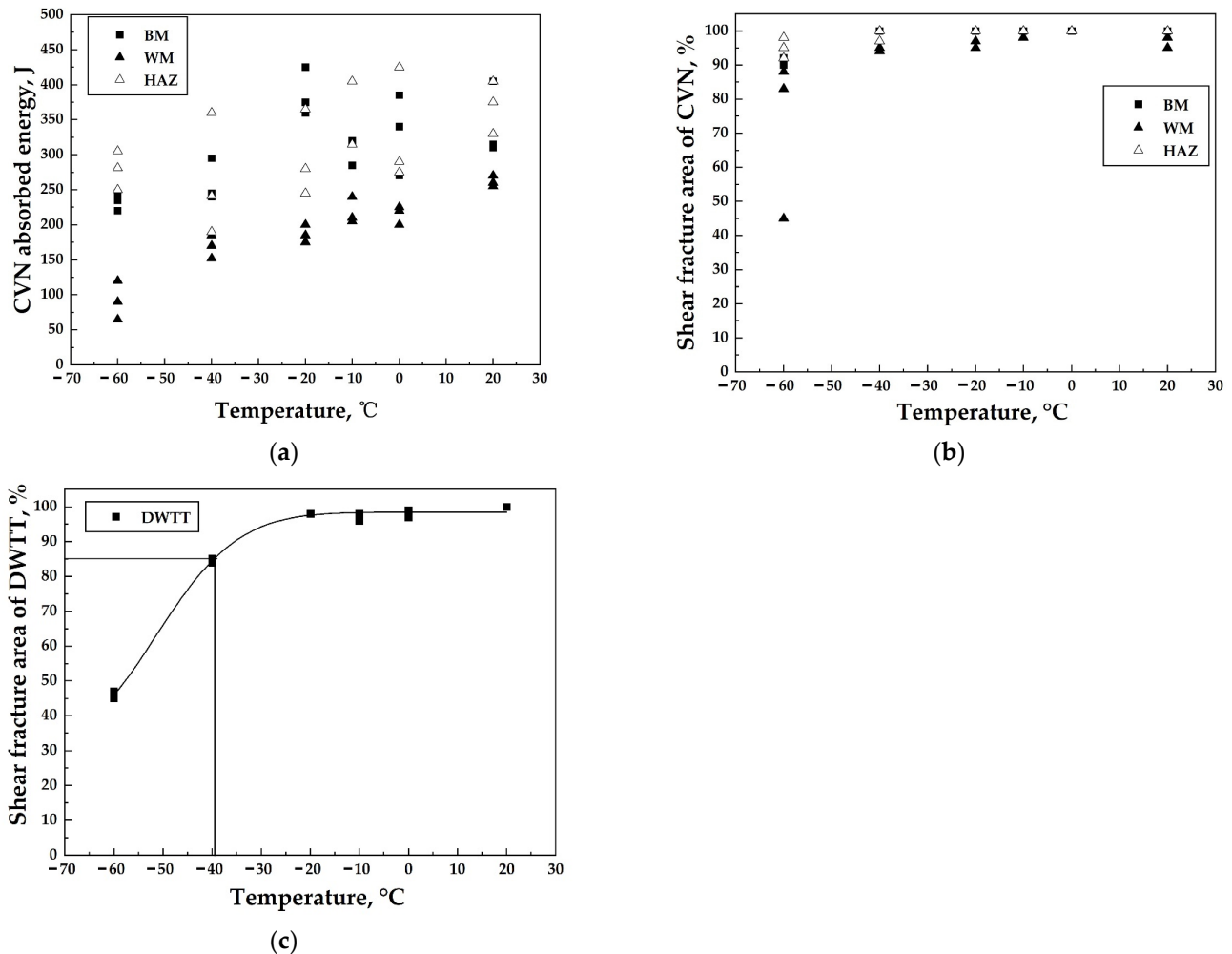


**Figure 4.** Series CVN and DWTT curves of BM, WM and HAZ. (a) CVN absorbed energy and (b) shear fracture area of CVN and (c) shear fracture area of DWTT.

### 3.2. Microstructure

TEM micrographs illustrating the microstructure of BM are presented in Figure 5. The microstructure consisted of polygonal ferrite (PF) plus lath bainite. PF microstructure with mobile dislocations induced by the shear process and volume expansion caused by the transformation from austenite to bainite (Figure 5a), guaranteeing the excellent deformability. Lath bainite contained high density tangled dislocations and substructures (Figure 5b), leading to the high strength.

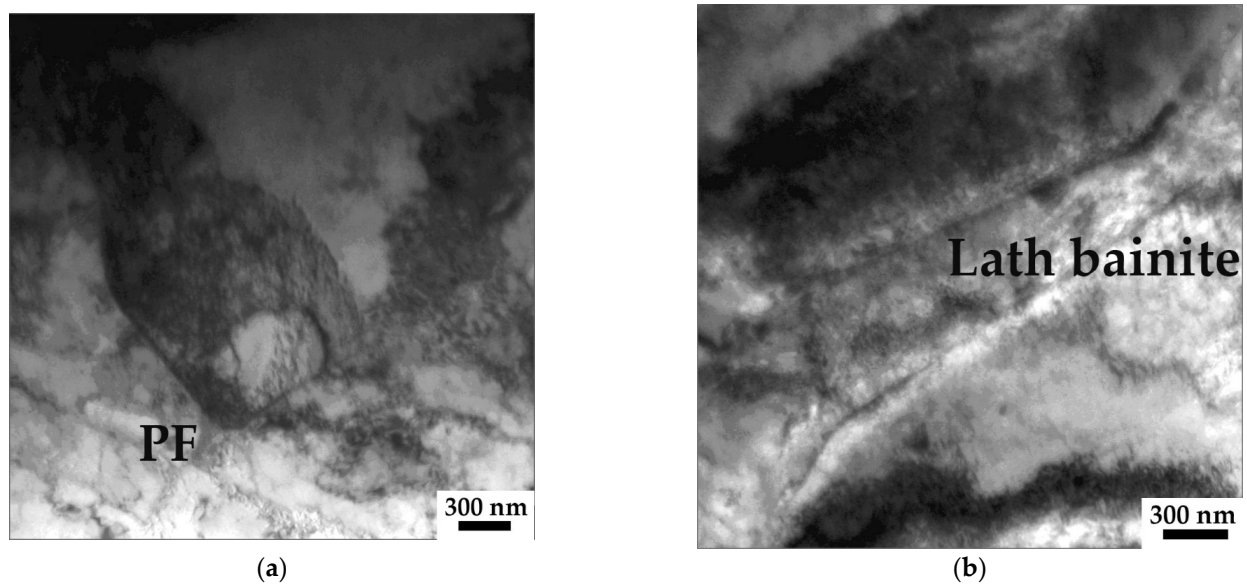


**Figure 5.** Bright field TEM micrographs illustrating the microstructure of the BM at location “1” in Figure 1a. (a) Polygonal ferrite (PF) containing high density of motile dislocations and (b) bainite plates containing high density of tangled dislocations.

SEM micrographs of HAZ are showed in Figure 6. Figure 6a shows the fusion line between the WM in the left and the CGHAZ in the right. The microstructure of the WM was mainly intragranular acicular ferrite (IAF) and a small amount of PF, pearlite and granular bainite (GB), showing the interlocked microstructures. IAF was a desirable microstructure in WM, whose laths divided the prior austenite grains into small regions before the forming of lower temperatures transforming microstructure [20–22], and hence leading to the grain refinement, guaranteeing the high strength, toughness and over matching requirements of the welded joint.

The microstructure of the CGHAZ was predominantly GB with distinct PAGBs and MA constituents of the blocky or stringer morphologies inside or along the PAGBs. GB contained a high carbon amount and large amount of lattice deficiencies resulting in high hardness and potential low CVN impact toughness [23]. Although impact toughness of the CGHAZ cannot be singly measured because of the limit of the little size, it can be deduced that the toughness behaviors of CGHAZ were worse than other regions of HAZ, due to the coarse microstructure [24].

The average grain size of FGHAZ was 7.14  $\mu\text{m}$ , which was much smaller than that of CGHAZ (20.87  $\mu\text{m}$ ). At the same time, many QF and PF were observed in FGHAZ, with the volume fraction up to 71.1%, accompanied by the obvious dropping in number of MA constituents (Figure 6b). While the microstructure of the CGHAZ was predominantly GB with high hardness, resulted in the obvious hardness increase by approximately 20 HV10 points, compared to that of FGHAZ, and potential low CVN impact toughness [12]. The ICHAZ microstructure with ferrite plus martensite/bainite was observed. During welding process, when the peak temperature decreased to  $A_{c1}$ - $A_{c3}$ , supersaturated solute carbons in the bainite in the BM microstructure precipitated, and then the austenite nucleated at these carbides, and grew in ferric matrix [25]. In successive cooling, austenite was transformed into martensite/bainite [26,27]. Due to the rapid heating and cooling during welding heat cycle, the equilibrium amount of the austenite can be not obtained, especially in the ICHAZ near SCHAZ, resulting in the distribution of martensite/bainite in a disperse state. In ICHAZ, from one boundary near FGHAZ to another boundary near SCHAZ, the volume fraction of martensite/bainite and the size of the ferrite grain decreased gradually from 28.94% and 9.97  $\mu\text{m}$  to 24.54% and 7.79  $\mu\text{m}$ , respectively, with the decrease in the peak temperature of the welding thermal cycles from  $A_{c3}$  to  $A_{c1}$  (Figure 6c,d), resulting

in the further decrease of the hardness from 228 HV10 to 182 HV10. In ICHAZ, the martensite/bainite distributed on the grain boundaries is usually regarded as the site of the crack initiation, which probably results the decrease of impact toughness.

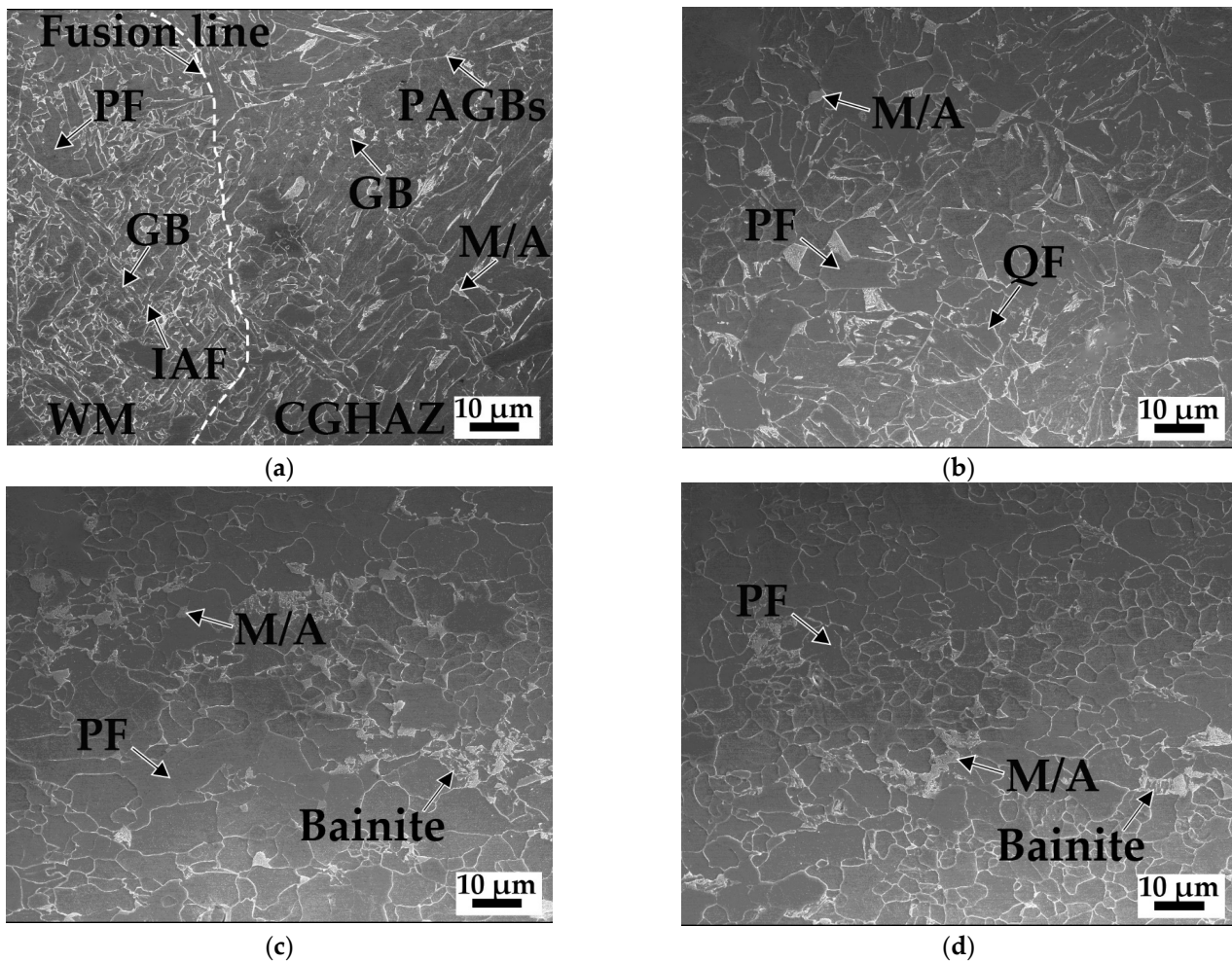


**Figure 6.** SEM micrographs of HAZ. (a) FL between CGHAZ and WM, (b) FGHAZ, (c) ICHAZ near FGHAZ and (d) ICHAZ near SCHAZ.

For V-notch of impact specimens through HAZ, potential low toughness of CGHAZ and ICHAZ may be suppressed by the FGHAZ with higher toughness. The impact toughness potentially increased in FGHAZ and decreased in CGHAZ and ICHAZ, which combined to cause the increase of the toughness in HAZ in this study [24,28].

Figure 7 shows the SEM micrographs of SCHAZ and BM. The SCHAZ with PF plus tempered bainite is similar to the BM with PF plus bainite. In SCHAZ, because of being exposed to the welding thermal cycles below  $A_{c1}$ , bainite occurred recovery and recrystallization [29], carbides precipitated from bainite and spheroided, and the dislocation density reduced, resulting in the decrease of the hardness of SCHAZ, compared to that of BM. Closer distance from the weld in SCHAZ, the higher the peak temperatures and the shorter the cooling times were. The combination of peak temperature and time produced different tempered effects, leading to the hardness in the range of 182 HV10 to 204 HV10. With increasing distance from the weld, the hardness of SCHAZ increased gradually until 226 HV10 in BM.



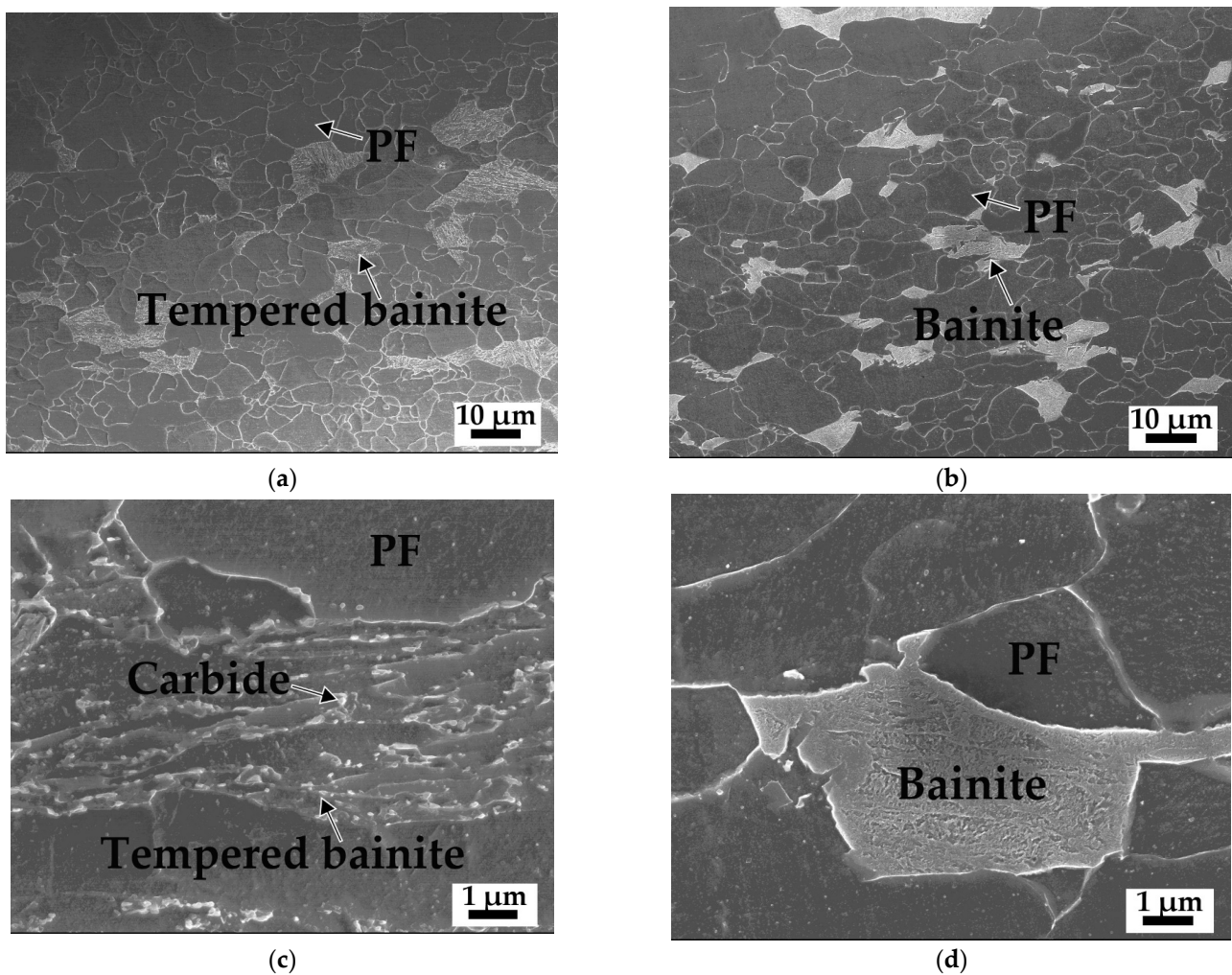


Figure 7. SEM micrographs of (a,c) SCHAZ and (b,d) BM of location “1” in Figure 1a.

#### 4. Discussion

##### 4.1. Thermodynamic Analysis of TiN and NbC Formation

The formation process of TiN and NbC was preceded by thermodynamic analysis. Ti preferentially combined with N to generate TiN [30]. The reaction formula and theoretical concentration product ( $K_{\text{TiN}}$ ) of the TiN in molten steel are shown in Equations (2) and (3) [31–33].



$$\log K_{\text{TiN}} = \log([\text{Ti}] \times [\text{N}]) = -15,218/T + 5.67 \quad (3)$$

Ti and N accumulated at the solidification front during the solidification process of molten steel, and with an increase in the solid fraction ( $f_s$ ), the concentrations of the Ti and N at the solidification front increased, as expressed by Equations (4) and (5) [33], respectively.

$$[\text{Ti}]_1 = [\text{Ti}]_0 \times (1 - f_s)^{k_{\text{Ti}}^{-1}}, \quad (4)$$

$$[\text{N}]_1 = [\text{N}]_0 / (1 - (1 - k_{\text{N}}) \times f_s) \quad (5)$$

In the formulas,  $[\text{Ti}]_1$ ,  $[\text{N}]_1$ ,  $[\text{Ti}]_0$ , and  $[\text{N}]_0$  represent the concentrations of Ti and N at the solidification front and their initial concentrations, respectively;  $k_{\text{Ti}}$  and  $k_{\text{N}}$  represent the

equilibrium distribution coefficients of Ti and N, at 0.33 and 0.48, respectively. The actual concentration of the product ( $Q_{\text{TiN}}$ ) of Ti and N in molten steel is expressed by Equation (6).

$$\log Q_{\text{TiN}} = \log([\text{Ti}]_0 \times [\text{N}]_0 \times (1 - f_s)^{k_{\text{Ti}}-1} / (1 - (1 - k_{\text{N}}) \times f_s)) \quad (6)$$

The temperature  $T$  of the solidification front can be expressed by Equation (7).

$$T = T_{\text{Fe}} - (T_{\text{Fe}} - T_1) / (1 - f_s \times (T_1 - T_s) / (T_{\text{Fe}} - T_s)) \quad (7)$$

In the formula,  $T_{\text{Fe}}$  is the melting point temperature of molten steel at 1809 K;  $T_1$  is the liquidus temperature at 1736 K; and  $T_s$  is the solidus temperature at 1792 K. JMatPro software was used to obtain  $T_1$  and  $T_s$ .

The thermodynamic curves according to Equations (3) and (6) are presented in Figure 8a. From the intersection of the curves, TiN began to precipitate at 0.96 of  $f_s$ . Substituting  $f_s$  into Equation (7), it is found that the TiN began to precipitate at 1747 K, which is close to  $T_s$ , leading to a small-sized TiN with better grain refinement effect in the steel.

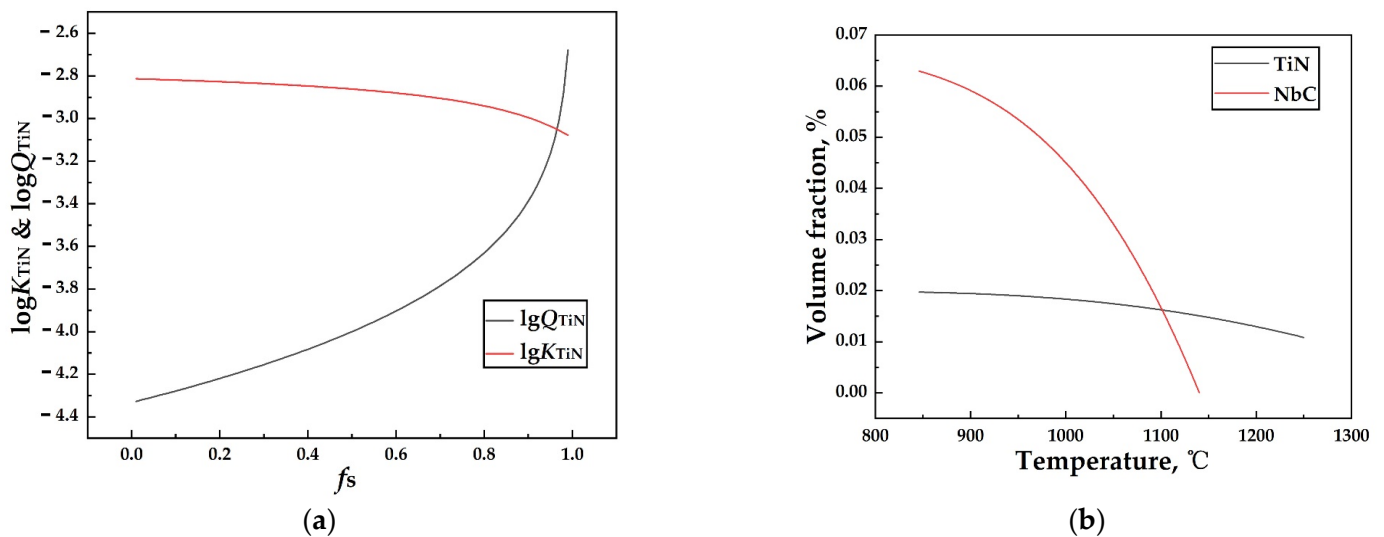


**Figure 8.** Thermodynamic analysis of TiN and NbC: (a) Relationship between  $k_{\text{TiN}}$  and  $Q_{\text{TiN}}$  of TiN inclusion and  $f_s$ , (b) variation of volume fraction ( $f$ ) of NbC and TiN with temperature.

The reaction formula and theoretical concentration product ( $(K_{\text{NbC}})_r$ ,  $(K_{\text{TiN}})_r$ ) of the NbC and TiN in austenite are shown in Equations (8), (9) and (11), and the stoichiometric ratio of NbC and TiN is shown in Equations (10) and (12).



$$\log (K_{\text{NbC}})_r = \log ([\text{Nb}] \times [\text{C}]_r) = 2.96 - 7510/T, \quad (9)$$

$$(0.059 - [\text{Nb}]) / (0.05 - [\text{C}]) = 7.735, \quad (10)$$

$$\log (K_{\text{TiN}})_r = \log ([\text{Ti}] \times [\text{N}]_r) = 0.32 - 8000/T, \quad (11)$$

$$(0.014 - [\text{Ti}]) / (0.0031 - [\text{N}]) = 3.419 \quad (12)$$

In the formulas,  $[\text{Nb}]$ ,  $[\text{C}]$ ,  $[\text{Ti}]$ , and  $[\text{N}]$  represent the concentrations of Nb, C, Ti, and N in austenite, respectively.

$f$  represents the volume fraction of NbC/TiN, which is shown in Equation (13).

$$f = (M - [M]) \times \frac{A_S}{A_M} \times \frac{d_{\text{Fe}}}{100 \times d_S} \quad (13)$$

$A_S$  and  $A_M$  are atomic weight of NbC/TiN and Nb/Ti, respectively.  $d_F$  and  $d_S$  are the density of Fe and NbC/TiN, at 7.875 and 7.803/5.398, respectively.

The variation of  $f$  of NbC and TiN with temperature according to Equations (9)–(13) is presented in Figure 8b. It is shown that NbC gradually dissolved in austenite with the increase of temperature until 1141 °C, at which NbC completely dissolved in austenite. At  $A_{c3}$  of 846 °C calculated using the following empirical Equation (14),  $f_{TiN}$  is 0.01971%, and  $f_{NbC}$  is 0.01085% at 1250 °C with 45% of TiN solution in austenite, compared with that at 846 °C. The  $A_{c1}$  is 714 °C calculated using the Equation (15).

$$A_{c3} (\text{°C}) = 881 - 206C - 15Mn - 26.5Cu - 20.1Ni + 53.1Si - 0.7Cr + 41.7V \quad (14)$$

$$A_{c1} (\text{°C}) = 751 - 16.3C - 27.5Mn - 5.5Cu - 5.9Ni + 34.9Si + 12.7Cr + 3.4Mo \quad (15)$$

#### 4.2. Influence of TiN and NbC on Microstructure of HAZ

As mentioned in Section 3.2, because of being exposed to successive heat inputs, the microstructure of the HAZ changed from one boundary to other boundary during welding. Due to different microstructures in the HAZ, the mechanical properties, including hardness, tensile properties and impact toughness can differ significantly in different regions, resulting in the significant property difference among HAZ specimens.

Most of NbC had been dissolved in the CGHAZ, due to the high peak temperature of 1100 °C- $T_s$  in welding thermal cycle. When the temperature rises to 1141 °C, NbC completely dissolved in steel (Figure 8b), which decreased the pinning to austenite grain boundary. However, the TiN precipitates did not dissolve completely in CGHAZ during the welding thermal cycles even at 1250 °C with 55% of TiN kept precipitating in steel, compared with that at 846 °C (Figure 8b), which can effectively refine the austenite grain [34].

Figure 9 shows the TEM micrograph of CGHAZ. TiN precipitates can still be found in CGHAZ subjected to the high peak temperature of 1100 °C- $T_s$  in welding thermal cycle, which is consistent with the precipitation behavior of TiN, shown in Figure 8b.

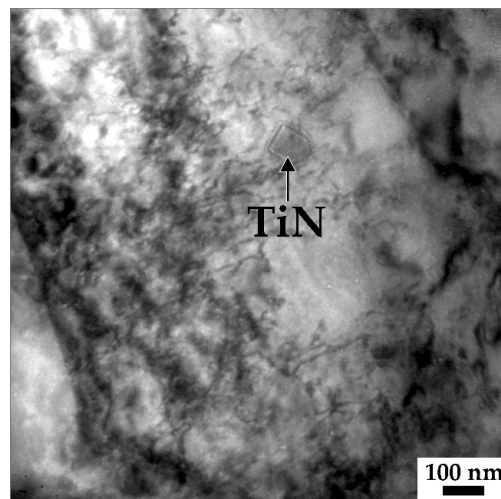


Figure 9. TEM micrograph of CGHAZ.

The CGHAZ microstructure was followed by FGHAZ microstructure with peak temperature between  $A_{c3}$  (846 °C) and 1100 °C, which has 0.06292–0.01663% of  $f_{NbC}$  (Figure 8b). The grain size of FGHAZ (7.14 μm) became much smaller than that of CGHAZ (20.87 μm), because of most of TiN and NbC without solution in this temperature range, which obviously refine the austenite grain.

During welding, the BM experiences different peak temperature produced by the welding thermal cycles. The ferrite plus martensite/bainite microstructure of BM was

heated between  $A_{c1}$  (714 °C) and  $T_s$  forming the HAZ containing CGHAZ, FGHAZ, ICHAZ, and SCHAZ. However, high CVN impact toughness of 345 J at  $-10$  °C and hardness in HAZ are obtained, which indicates that the excellent mechanical properties of BM would not be seriously deteriorated during the welding thermal cycles with the reasonable addition of Ti and Nb.

## 5. Conclusions

In the present study, the mechanical properties and microstructure of X70 pipeline steel with strain-based design were evaluated, and the following conclusions could be reached.

(1) All the specimens tested in present work met the strength and ductility properties requirements of X70 grade pipeline steel with strain-based design. BM with a dual-phase microstructure exhibited continuous yielding behavior with an average longitudinal yield strength of 486 MPa, average tensile strength of 642 MPa, average yield ratio of 0.76 and average uniform elongation of 9.4%, indicating high strength and deformability. WM transverse tensile strength is 645 MPa, higher than 630 MPa of BM, meeting the over matching requirement, and the position of specimen fracture was in the BM.

(2) The SA of CVN at  $-10$  °C was  $>97\%$  in the BM, WM, and HAZ. The CVN absorbed energy was  $>285$  J in BM,  $>315$  J in HAZ and  $>205$  J in WM. Adequate CVN toughness and adequate DWTT SA ensured the avoidance of brittle fracture propagation and the control of ductile fracture propagation.

(3) The microstructure of X70 pipeline steel with strain-based design consisted of ferrite plus bainite. Polygonal ferrite microstructure with mobile dislocations guaranteed the excellent deformability. Lath bainite with high density tangled dislocations and substructures led to the high strength. This kind of microstructure still keeps the high toughness during welding processes.

(4) The microstructure of the WM was mainly IAF, guaranteeing high strength, toughness and over matching requirements of the welded joint. The ferrite plus martensite/bainite microstructure of BM was heated between  $A_{c1}$  and  $T_s$  forming the HAZ containing CGHAZ, FGHAZ, ICHAZ, and SCHAZ. However, the high CVN impact toughness of 345 J at  $-10$  °C and hardness in HAZ are obtained, which indicates that the excellent mechanical properties of BM would not be seriously deteriorated during the welding thermal cycles with the reasonable addition of Ti and Nb.

**Author Contributions:** Conceptualization, X.Z., D.L., Y.D., R.L., J.J., X.L. and Z.W.; Methodology, X.Z., D.L., Y.D., R.L., J.J., X.L. and Z.W.; Software and Experimental Validation, D.L., Y.D. and R.L.; Formal Analysis and Investigation, X.Z., D.L., Y.D. and R.L.; Resources, X.Z.; Data Curation, X.Z., D.L., Y.D. and R.L.; Writing—Original Draft Preparation, D.L.; Writing—Review and Editing, Z.W. and X.Z.; Supervision, X.L., Z.W. and X.Z.; Project Administration, X.Z. and J.J.; Funding Acquisition, X.Z. All authors have read and agreed to the published version of the manuscript.

**Funding:** This research was funded by Henan Provincial Science and Technology Cooperation Project China (grant no. 182106000016) and the Key R & D and Promotion Special Project of Henan Province (no. 212102210444).

**Institutional Review Board Statement:** Not applicable.

**Informed Consent Statement:** Not applicable.

**Data Availability Statement:** Data are contained within the article.

**Acknowledgments:** The authors gratefully acknowledge the financial support provided by Nanjing Iron & Steel Co., Ltd.

**Conflicts of Interest:** The authors declare no conflict of interest.

## References

1. Tu, X.Y.; Shi, X.B.; Yan, W.; Li, C.S.; Shi, Q.Q.; Shan, Y.Y.; Yang, K. Tensile deformation behavior of ferrite-bainite dual-phase pipeline steel. *Mater. Sci. Eng. A* **2022**, *831*, 142230. [[CrossRef](#)]
2. Wan, X.L.; Wu, K.M.; Xia, Z.H. The effect of microstructure on properties of high deformation pipeline steel X70. *Adv. Mater. Res.* **2013**, *2384*, 182–185. [[CrossRef](#)]
3. Li, R.T.; Zuo, X.R.; Hu, Y.Y.; Wang, Z.W.; Hu, D.X. Microstructure and properties of pipeline steel with a ferrite/martensite dual-phase microstructure. *Mater. Charact.* **2011**, *62*, 801–806. [[CrossRef](#)]
4. Zheng, X.F.; Kang, Y.L.; Meng, D.L.; AN, S.Y.; Xia, D.X. Effect of cooling start temperature on microstructure and mechanical properties of X80 high deformability pipeline steel. *J. Iron Steel Res. Int.* **2011**, *18*, 42–46, 71. [[CrossRef](#)]
5. Zhang, X.Y.; Gao, H.L.; Zhang, X.Q.; Yang, Y. Effect of volume fraction of bainite on microstructure and mechanical properties of X80 pipeline steel with excellent deformability. *Mater. Sci. Eng. A* **2012**, *531*, 84–90. [[CrossRef](#)]
6. Machado, F.R.D.S.; Ferreira, J.C.; Rodrigues, M.V.G.; Lima, M.N.D.S.; Loureiro, R.D.C.P.; Siciliano, F.; Silva, E.S.; Reis, G.S.; Sousa, R.C.D.; Aranas, C., Jr; et al. Dynamic ferrite formation and evolution above the Ae<sub>3</sub> temperature during plate rolling simulation of an API X80 steel. *Metals* **2022**, *12*, 1239. [[CrossRef](#)]
7. Suwanpinij, P.; Togobytska, N.; Prah, U.; Weiss, W.; Hömberg, D.; Bleck, W. Numerical cooling strategy design for hot rolled dual phase steel. *Steel Res. Int.* **2010**, *81*, 1001–1009. [[CrossRef](#)]
8. Tu, X.Y.; Shi, X.B.; Shan, Y.Y.; Yan, W.; Shi, Q.Q.; Li, C.S.; Yang, K. Tensile deformation damage behavior of a high deformability pipeline steel with a ferrite and bainite microstructure. *Mater. Sci. Eng. A* **2020**, *793*, 139889. [[CrossRef](#)]
9. Zuo, X.R.; Li, R.T. Research of strain aging in pipeline steel with a ferrite/martensite dual phase microstructure. *Steel Res. Int.* **2015**, *86*, 163–168. [[CrossRef](#)]
10. Hu, Y.Y.; Zuo, X.R.; Li, R.T.; Wang, Z.W. Comparison of two different rolling processes on microstructure and properties of ferrite-bainite dual-phase pipeline steels. *Adv. Mater. Res.* **2011**, *197–198*, 724–729. [[CrossRef](#)]
11. Qi, X.N.; Huan, P.C.; Wang, X.N.; Liu, Z.G.; Shen, X.J.; Gao, Y.; Di, H.S. Effect of root welding heat input on microstructure evolution and fracture mechanism in intercritically reheat-coarse grained heat-affected zone of X80 pipeline steel. *Mater. Today Commun.* **2022**, *31*, 103413. [[CrossRef](#)]
12. Lan, L.Y.; Qiu, C.L.; Zhao, D.W.; Gao, X.H.; Du, L.X. Microstructural characteristics and toughness of the simulated coarse grained heat affected zone of high strength low carbon bainitic steel. *Mater. Sci. Eng. A* **2021**, *529*, 192–200. [[CrossRef](#)]
13. Zhu, Z.X.; Kuzmikova, L.; Li, H.J.; Barbaro, F. Effect of inter-critically reheating temperature on microstructure and properties of simulated inter-critically reheated coarse grained heat affected zone in X70 steel. *Mater. Sci. Eng. A* **2014**, *605*, 8–13. [[CrossRef](#)]
14. Ringinen, D.A.; Chastukhin, A.V.; Khadeev, G.E.; Efron, L.I.; Il'inskii, V.I. Evolution of austenite grain structure and microalloying element precipitation during heating of steel of strength class K65 (X80) for rolling. *Metallurgist* **2014**, *57*, 996–1004. [[CrossRef](#)]
15. Wei, R.; Shang, C.J.; Wu, K.M. Grain refinement in the coarse-grained region of the heat-affected zone in low-carbon high-strength microalloyed steels. *Int. J. Miner. Metall. Mater.* **2010**, *17*, 737–741. [[CrossRef](#)]
16. Fan, L.F.; Yan, J.X.; Gao, Y.; Yun, J.B. Research on deformation characteristics of JCOE forming in large diameter welding pipe. *Adv. Manuf.* **2016**, *4*, 268–277. [[CrossRef](#)]
17. Batalov, G.S.; Lunev, A.A.; Radionova, L.V.; Lezin, V.D. Development of new methods for the production of large-diameter double-seam pipes. *Solid State Phenom.* **2021**, *316*, 538–548. [[CrossRef](#)]
18. Chatzopoulou, G.; Antoniou, K.; Karamanos, S.A. Numerical simulation of JCO pipe forming process and its effect on the external pressure capacity of the pipe. In Proceedings of the ASME 2017 36th International Conference on Ocean, Offshore and Arctic Engineering, Trondheim, Norway, 25–30 June 2017; Volume 5B, p. 8. [[CrossRef](#)]
19. *API SPECIFICATION 5 L*; Specification for line pipe forty-fourth edition; API Publishing Services: Washington, DC, USA, 2013; pp. 74–180.
20. Jiang, M.; Wang, X.H.; Hu, Z.Y.; Wang, K.P.; Yang, C.W.; Li, S.R. Microstructure refinement and mechanical properties improvement by developing IAF on inclusions in Ti-Al complex deoxidized HSLA steel. *Mater. Charact.* **2015**, *108*, 58–67. [[CrossRef](#)]
21. Zhang, J.; Xin, W.B.; Luo, G.P.; Wang, R.F.; Meng, Q.Y. Significant Influence of Welding Heat Input on the Microstructural Characteristics and Mechanical Properties of the Simulated CGHAZ in High Nitrogen V-Alloyed Steel. *High Temp. Mater. Proc.* **2020**, *39*, 33–44. [[CrossRef](#)]
22. Wu, B.B.; Wang, Z.Q.; Shang, C.J.; Yu, Y.S.; Yang, Z.G.; Zhang, C. A route to produce toughened acicular ferrite with equivalent hardness as martensite: The combined effect of elements segregation and pre-transformed allotriomorphic ferrite. *Mater. Charact.* **2021**, *182*, 111528. [[CrossRef](#)]
23. Li, C.W.; Wang, Y.; Han, T.; Han, B.; Li, L.Y. Microstructure and toughness of coarse grain heat-affected zone of domestic X70 pipeline steel during in-service welding. *J. Mater. Sci.* **2011**, *46*, 727–733. [[CrossRef](#)]
24. Dong, Y.F.; Liu, D.H.; Hong, L.; Liu, J.J.; Zuo, X.R. Correlation between microstructure and mechanical properties of welded joint of X70 submarine pipeline steel with heavy wall thickness. *Metals* **2022**, *12*, 716. [[CrossRef](#)]
25. Yi, J.J.; Kim, I.S.; Choi, H.S. Austenitization during intercritical annealing of an Fe-C-Si-Mn dual-phase steel. *Metall. Trans. A* **1985**, *16*, 1237–1245. [[CrossRef](#)]
26. Kabanov, A.; Korpala, G.; Kawalla, R.; Prah, U. Effect of hot rolling and cooling conditions on the microstructure, MA constituent formation, and pipeline steels mechanical properties. *Steel Res. Int.* **2018**, *90*, 1800336. [[CrossRef](#)]

27. Regier, R.W.; Reguly, A.; Matlock, D.K.; Choi, J.K.; Speer, J.G. Effects of austenite conditioning and transformation temperature on the bainitic microstructure in linepipe steels. *Mater. Sci. For.* **2014**, *783–786*, 85–90. [[CrossRef](#)]
28. Chen, X.W.; Liao, B.; Qiao, G.Y.; Gu, Y.; Wang, X.; Xiao, F.R. Effect of Nb on mechanical properties of HAZ for high-Nb X80 pipeline steels. *J. Iron Steel Res. Int.* **2013**, *20*, 53–60. [[CrossRef](#)]
29. Wu, H.B.; Yang, S.W.; Guo, A.M.; Yuan, S.Q.; Shang, C.J.; He, X.L. Thermo-stability of ultra-fine non-equilibrium microstructures. *J. Univ. Sci. Technol. B* **2004**, *11*, 338–342. [[CrossRef](#)]
30. Wu, X.; Zuo, X.R.; Zhao, W.W.; Wang, Z.Y. Mechanism of TiN fracture during the tensile process of NM500 wear-resistant steel. *Acta Metall. Sin.* **2020**, *56*, 129–136. [[CrossRef](#)]
31. Wang, L.; Xue, Z.-L.; Zhu, H.; Lei, J.-L. Thermodynamic analysis of precipitation behavior of Ti-bearing inclusions in SWRH 92A tire cord steel. *Results Phys.* **2019**, *14*, 102428. [[CrossRef](#)]
32. Li, N.; Wang, L.; Xue, Z.L.; Li, C.Z.; Huang, A.; Wang, F.F. Study of precipitation and growth processes of Ti-bearing inclusions in tire cord steel. *Results Phys.* **2020**, *16*, 102929. [[CrossRef](#)]
33. Liu, D.H.; Wang, Z.Y.; Liu, J.J.; Wang, Z.L.; Zuo, X.R. Study of the fracture behavior of TiN and TiC inclusions in NM550 wear-resistant steel during the tensile process. *Metals* **2022**, *12*, 363. [[CrossRef](#)]
34. Zhu, Y.; Lu, Y.M.; Huang, C.W.; Liang, Y.L. The effect of TiN inclusions on the fracture mechanism of 20CrMnTi steel with lath martensite. *Mater. Res. Express.* **2020**, *7*, 036509. [[CrossRef](#)]